doi:10.26443/seismica.v4i1.1336

SEISMICA

An unexplained tsunami: Was there megathrust slip during the 2020 $\mathrm{M_w}$7.6 Sand Point, Alaska, earthquake?

Sean R. Santellanes * [1], **Dara E. Goldberg** [2], **Pablo Koch**[3], **Diego Melgar** [1], **William L. Yeck** [2], **Brendan W. Crowell** [4,5], **Jiun-Ting Lin** [6]

[1]Department of Earth Sciences, University of Oregon, Eugene, OR, USA, [2]U.S. Geological Survey, Geologic Hazards Science Center, Golden, CO, USA, [3]Centro Sismológico Nacional de Chile, Santiago, Chile, [4]Department of Earth and Space Sciences, University of Washington, Seattle, WA, USA, [5]School of Earth Sciences, The Ohio State University, Columbus, Ohio, USA, [6]Lawrence Livermore National Laboratory, Livermore, CA, USA

Author contributions: *Conceptualization*: SRS. *Methodology*: DEG, DM, SRS. *Software*: All authors. *Validation*: DEG, SRS. *Formal Analysis*: DEG, DM, SRS, WLY. *Investigation*: All authors. *Resources*: All authors. *Writing - Original draft*: SRS. *Writing - Review & Editing*: All authors. *Visualization*: DEG, PK, DE, SRS. *Supervision*: DEG, DM. *Funding acquisition*: DM.

Abstract On October 19, 2020, the moment magnitude ($\mathrm{M_w}$) 7.6 Sand Point earthquake struck south of the Shumagin Islands in Alaska. Moment tensors indicate the earthquake was primarily strike-slip, yet the event produced an enigmatic tsunami that was larger and more widespread than expected for an earthquake of that magnitude and mechanism. Using a suite of hydrodynamic, seismic, and geodetic modeling techniques, we explore plausible causes of the tsunami. We find that strike-slip models consistent with the moment tensor orientation cannot produce the observed tsunami. Hydrodynamic inversion of sea surface deformation from deep ocean and tide gauge data indicate seafloor deformation more closely matches a megathrust, rather than a strike-slip, source. Static slip inversions using sea level and Global Navigation Satellite System data allow for a portion of co-seismic megathrust slip that can explain tsunamigenesis. Combining all available geophysical datasets to model the kinematic rupture, we show that considerable, relatively slow, megathrust slip is allowable in the Shumagin segment, concurrent with strike-slip faulting. We hypothesize that the slow megathrust rupture does not contribute much seismic radiation allowing it to previously go unnoticed with traditional seismic monitoring.

Production Editor:
Gareth Funning
Handling Editor:
Wenbin Xu
Copy & Layout Editor:
Abhineet Gupta

Signed reviewer(s):
Kejie Chen
Chao An

Received:
March 22, 2024
Accepted:
November 14, 2024
Published:
February 10, 2025

Non-technical summary On October 19, 2020, a magnitude 7.6 earthquake occurred south of Alaska's Shumagin Islands. Seismic instruments in Alaska and globally observed the earthquake to be a strike-slip earthquake, characterized by lateral (as opposed to vertical) fault motion. That lack of vertical motion generally results in only small, localized tsunamis. However, this earthquake produced a tsunami that was observed as far away as Hawaii. In this work, we confirm that a simple strike-slip earthquake cannot generate the observed far-reaching tsunami. Instead, ocean height observations are consistent with a typical tsunamigenic megathrust earthquake, characterized by vertical motion at the subduction interface. The combination of seismic, geodetic, and ocean height observations allow for concurrent strike-slip and megathrust rupture wherein the megathrust rupture occurred at comparatively slow speeds. We hypothesize that these slow rupture speeds are why the megathrust portion of this earthquake went undetected by seismic instruments.

1 Introduction

Tsunamis are most often the result of earthquake sources at subduction zones. Subduction zone fault slip is a key process for tsunamigenesis that can produce large enough vertical motion to result in hazardous waves. The Shumagin segment of the Alaskan subduction zone (Figure 1) has been characterized as an area largely devoid of great earthquakes ($\mathrm{M_w} \geq 8.0$) for at least the past 100 years (Davies et al., 1981). This may be due to the location being in transition between the fully creeping Sanak segment to the west and the fully locked Semidi segment to the east (Li and Freymueller, 2018). The Shumagin segment's seismic history is in stark contrast to its neighboring segments; great earthquakes have been observed in the Sanak segment (1946 $\mathrm{M_w}$8.6) and the Semedi segment (1938 $\mathrm{M_w}$8.3) in the past century, each producing large, devastating tsunamis (Davies et al., 1981; Witter et al., 2014; Li and Freymueller, 2018). Meanwhile, the last suspected great earthquake in the Shumagin segment is commonly thought to have occurred in 1788; however, geologic observations are more consistent with two earthquakes between $\mathrm{M_w}$7.7–8.1 occurring under a month apart (Witter et al., 2014).

The October 19, 2020, $\mathrm{M_w}$7.6 (seismic moment ($\mathrm{M_o}$) = 2.82×10^{20} N m) Sand Point earthquake was the second of three large earthquakes to affect the Alaskan Peninsula over a 12-month period. First, the July 22, 2020, $\mathrm{M_w}$7.8 ($\mathrm{M_o} = 6.91 \times 10^{20}$ N m) Simeonof earthquake occurred on the subduction zone fault interface near

*Corresponding author: ssantel2@uoregon.edu

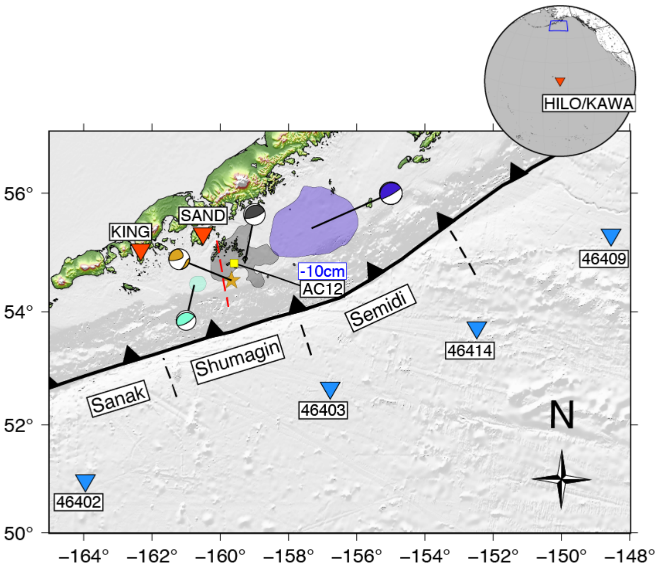

Figure 1 The study area, offshore of the Alaskan Peninsula. Demarcations for the Sanak, Shumagin, and Semidi segments from Liu et al. (2020) are shown with dashed black lines. The 2020 Simeonof rupture zone is shown in black (Crowell and Melgar, 2020); the 2021 Chignik rupture zone is shown in dark blue (USGS Earthquake Hazards Program, 2017); and the July 2023 Sand Point rupture zone is shown in aquamarine. The W-phase centroid moment tensors (WCMT) for Simeonof, Chignik, and July 2023 Sand Point are shown in the same colors as their rupture zones. The surface projection of the U.S. Geological Survey National Earthquake Information Center (USGS-NEIC) finite fault plane for the 2020 Sand Point earthquake is delineated by a dashed red line (USGS Earthquake Hazards Program, 2017). The epicenter and WCMT for the 2020 Sand Point earthquake are shown in gold. The King Cove (KING) and Sand Point (SAND) coastal sea level stations are shown as red triangles. Deep-ocean Assessment and Reporting of Tsunamis (DART) stations are shown as light blue triangles. Global Navigation Satellite System (GNSS) station AC12 (yellow square) is shown to have undergone $10\,\mathrm{cm}$ of subsidence during the 2020 Sand Point earthquake. The inset shows the locations of the coastal sea level stations (HILO/KAWA) in Hawaii (red triangles) and the outline of the main study area in blue. This map was constructed using GMT 6 (Wessel et al., 2019).

Simeonof Island (Figure 1, Crowell and Melgar, 2020). It produced a small tsunami with a $\sim 30\,\mathrm{cm}$ maximum amplitude (relative to typical sea level) at the nearby Sand Point, Alaska, coastal sea level station (Larson et al., 2021; Liu et al., 2022) and was barely measurable ($< 1\,\mathrm{cm}$ amplitude) at the Deep-ocean Assessment and Reporting of Tsunamis (DART) stations in the surrounding area.

In contrast, the $\mathrm{M_w}$7.6 Sand Point earthquake produced a tsunami with maximum amplitude of $76\,\mathrm{cm}$ at the same Sand Point coastal sea level station and a $\sim 30\,\mathrm{cm}$ maximum amplitude at the Hilo, Hawaii, coastal sea level station more than $3800\,\mathrm{km}$ away. The Sand Point tsunami was also recorded clearly by four DART stations (1–$4\,\mathrm{cm}$ amplitudes; Figure 2d) (Titov et al., 2005). The causative fault plane of this earthquake, based on the U.S. Geological Survey (USGS) National Earthquake Information Center (NEIC) W-Phase centroid moment tensor (WCMT), was a north-striking, $49°$ east-dipping, right-lateral, strike-slip fault with a 71% double-couple component (Figure 1). Strike-slip earthquakes typically do not produce large enough vertical deformation to generate tsunamis with amplitudes $> 30\,\mathrm{cm}$ in the near- or far-field. It is therefore enigmatic that the Sand Point event produced a substantially larger local and trans-oceanic tsunami than the Simeonof event, given that (1) it is ~2.5 times smaller by scalar moment, and (2) it has a strike-slip, rather than dip-slip, mechanism. The peculiar nature of the Sand Point earthquake's tsunami was highlighted again by the July 29, 2021, $\mathrm{M_w}$8.2 (seismic moment ($\mathrm{M_o}$) $= 2.36 \times 10^{21}\,\mathrm{N\,m}$) Chignik, Alaska, earthquake. The Chignik earthquake was a low angle thrust event and produced a similar trans-oceanic tsunami to the Sand Point earthquake, despite its larger magnitude and rupture area (Liu et al., 2022). Comparison to the tsunamis generated by these larger magnitude megathrust events indicates that additional factors must be contributing to the Sand Point earthquake's tsunami generation.

2 The incompatibility of a strike-slip source

2.1 USGS model

To test the hypothesis that strike-slip activation alone is insufficient to generate the observed Sand Point tsunami, we model the vertical seafloor deformation implied by the USGS finite fault model (model U0, Table 1) using a dislocation in an elastic half-space (Okada, 1985) and forward model the resulting tsunami waves using GeoClaw (LeVeque et al., 2011). GeoClaw solves the non-linear shallow-water equations using adaptive mesh refinement so that areas of high tsunami complexity, such as the coastal sea level station locations, can be refined to higher discretization. We use the Shuttle Radar Topography Mission 15 ($450\,\mathrm{m}$ pixels) for the model domain (Figure 1) (Tozer et al., 2019). We also use 1/3 arcsec ($\sim 10\,\mathrm{m}$ pixels) bathymetry/topography to provide greater detail for the areas around the coastal sea level stations. The tsunami simulations are run at 4 levels of mesh refinement starting at 5 arcmin ($\sim 7.5\,\mathrm{km}$) and ending at 3 arcsecs ($\sim 90\,\mathrm{m}$). We choose to use GeoClaw's kinematic rupture feature for all models for faithful comparisons amongst them.

We prescribe Gaussian-shaped sea surface deformation unit source areas in a two-dimensional grid with $10\,\mathrm{km}$ spacing across the region of interest; 428 sources in total (Figure S1). These unit source areas have an amplitude of $1\,\mathrm{m}$ and a standard deviation of $5\,\mathrm{km}$. The Gaussian nature of the tsunami source elements ensures that they overlap at the margins, such that smooth variations of sea surface displacements can be expressed with a sum of these discrete sources. Each tsunami source element is run independently in GeoClaw to compute the Green's function from each source to each of eight observing stations: two near-field coastal sea level stations on the Aleutian Islands

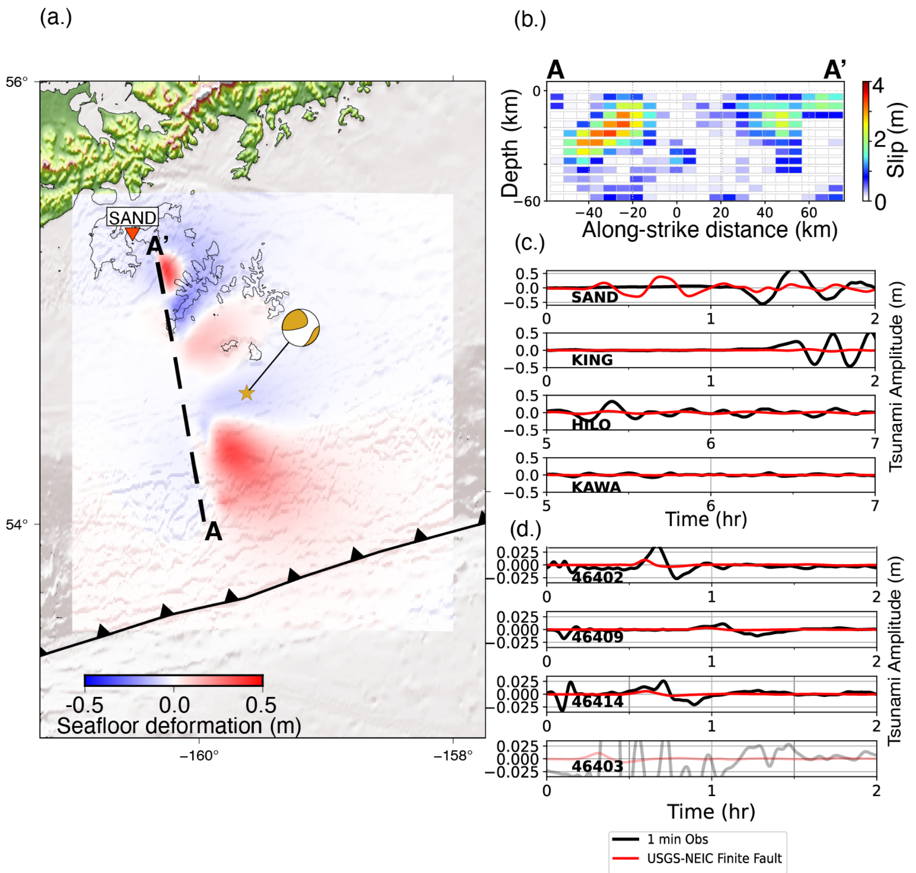

Figure 2 (a.) Map showing the vertical deformation resulting from the U.S. Geological Survey National Earthquake Information Center (USGS-NEIC) finite fault model (model U0). The dashed black line from A–A' is the surface projection of the causative fault plane, as inferred by the USGS-NEIC. The hypocenter (star) and W-phase centroid moment tensors (WCMT) are shown in gold. (b.) USGS-NEIC finite fault solution. (c.) The observed (black) and modeled (red) tsunami waveforms at coastal sea level stations. (d.) The observed (black) and modeled (red) tsunami waveforms at Deep-ocean Assessment and Reporting of Tsunamis (DART) stations. DART station 46403 is shown with slightly muted colors to indicate that it was affected by Rayleigh wave contamination. This map was constructed using GMT 6 (Wessel et al., 2019).

Model name	Segments	Data types	Allowable rise times	RMSE(s) [cm]
USGS-NEIC (U0)	SS	Teleseismic	N/A	9.0*
Static (S1)	SS	DART, CSLS, SGNSS	N/A	S1a:3.8* S1b:4.7*
Hydrodynamic (H0)	N/A	DART, CSLS	N/A	3.0*
Static (S2)	SS,MT	DART, CSLS, SGNSS	N/A	S2a: 82.3† S2b: 77.8†
Kinematic (K1)	SS, MT	DART	"Standard" (0–30 s)	4.0*
Kinematic (K2)	SS, MT	DART, SGNSS, HRGNSS, Teleseismic, STR	"Long" (0–60 s)	4.1*
Kinematic (K3)	SS, MT	DART, SGNSS, HRGNSS, Teleseismic, STR	MT: "Very Long" (0–120 s) SS: "Standard" (0–30 s)	4.2*

Table 1 The attributes of the inversions considered in this study. SS is strike-slip; MT is megathrust; CSLS is coastal sea level station; SGNSS is static Global Navigation Satellite System (GNSS); HRGNSS is high-rate GNSS; and STR is strong motion accelerometer. * denotes unweighted root mean squared error (RMSE) and †denotes weighted RMSE. N/A means not available.

(Sand Point and King Cove), two far-field coastal sea level stations in Hilo and Kawaihae, respectively, and four DART stations (Figure 1, Titov et al., 2005).

The vertical seafloor deformation pattern derived from the USGS strike-slip model has a peak subsidence of $0.2\,\mathrm{m}$ and a peak uplift of $0.4\,\mathrm{m}$ (Figure 2a), which is insufficient to produce the observed tsunami amplitudes (Figure 2c, d). The unweighted root mean squared error (RMSE) of the tsunami waveforms is $9.0\,\mathrm{cm}$. Not only is the modeled amplitude at the Sand Point coastal sea level station much smaller than the recorded amplitude ($0.4\,\mathrm{m}$ versus $1.3\,\mathrm{m}$ trough to crest), the forward-modeled tsunami also arrives ∼1 hour earlier than the observed tsunami. Although timing discrepancies are expected at far-field sites due to unmodeled effects of the compressional seafloor (Tsai et al., 2013), the large timing discrepancy at the near-field Sand Point site indicates that this strike-slip model does not accurately represent the tsunamigenic deformation.

The USGS model itself has unphysical qualities that indicate it is a poor representation of the true earthquake source. The published model on the USGS event page has the hypocentral depth at 40 km, yet it strongly prefers slip at shallower depths that extends through the top of the slab (https://earthquake.usgs.gov/earthquakes/eventpage/us6000c9hg/executive, last accessed July 17, 2024). In addition, this model includes only teleseismic broadband observations and does not directly consider the tsunami signal. It is therefore expected that the USGS model is incompatible with the tsunami observations.

2.2 Joint model of on-shore and off-shore observations

We perform an additional slip inversion on the strike-slip fault orientation using observations of both the earthquake and the tsunami: DART, near-field coastal sea level, and 11 onshore static Global Navigation Satellite System (GNSS) surface displacements estimated by Central Washington University (Herring et al., 2016). We de-tide the coastal sea level observations and model synthetics with a bandpass filter from 5 min to 120 min. We apply a simple cross-correlation time shift to the synthetic data at the Hawaii coastal sea level stations to correct the far-field travel time error introduced by unmodeled effects from a compressible seafloor (Tsai et al., 2013). Tsunami propagation in shallow water is nonlinear, so only the first ∼1–1.5 wavelengths can be reliably considered; the nonlinearity makes later arrivals too difficult to account for in linear inversions (Melgar and Bock, 2013; Yue et al., 2015). DART station observations are typically sampled at 15 min intervals; however, the earthquake signal caused these stations to switch into "event mode", meaning they are temporarily sampled between 15 s and 1 min. We de-tide the DART observations and model synthetics with a bandpass filter from 5 min to 120 min. DART station data are recorded by a bottom pressure recorder. Seismic arrivals, such as Rayleigh waves and acoustic phases, introduce pressure signals that are separate from tsunami energy. As a result, it is important to mask out these earthquake signals and use only the portions of the waveform that reflect the tsunami itself. At DART station 46403 (Figure 1), the tsunami's arrival overlapped with seismic/acoustic signals, and therefore that station could not be used in this study's inversions. Regardless, the forward models in this study estimate the tsunami signal at all four DART station locations. We down-weight the King Cove coastal sea level station and DART station 46402 relative to the remaining sites because those observations appear to include an additional non-tectonic source (discussed in Section 5).

We use the MudPy slip inversion code (Melgar and Bock, 2013), regularized using a zeroth order Tikhonov approach and selecting the optimal regularization parameter from the L-curve criterion. The weighting scheme for the geodetic and coastal sea level data follows Melgar et al. (2016), allotting importance only to the linear portion of the waveform data. DART station and static GNSS data were weighted 10 times higher than the coastal sea level station data. We use the one-dimensional crustal velocity model (Pasyanos et al., 2014) to calculate the static Green's functions for the GNSS stations. Initially, we constrain the model to the USGS magnitude (model S1a, Figure 3a, Table 1), resulting in tsunami waveform fits with an average unweighted RMSE of 3.8 cm (Table 1). Next, we relax the moment constraint to test whether a larger magnitude strike-slip event can account for the observed tsunami signals (model S1b, Figure 3b, Table 1). Model S1b prefers an M_w8.0 source and results in degradation of the tsunami waveform fits (Figure 3c) with an unweighted RMSE of 4.7 cm. These results bolster the interpretation that a single, planar strike-slip fault with the geometry of the USGS WCMT cannot be the sole source of the observed tsunami.

3 Deformation requirements of the observed tsunami

Given that the WCMT strike-slip geometry cannot generate the observed tsunami, we use coastal sea level and DART data to invert directly for the sea floor deformation required to produce the observed tsunami signals, independent of a slip distribution. We refer to this hydrodynamic model as model H0 (Table 1). This approach is useful because it requires few assumptions and directly solves for the required hydrodynamic initial condition, the seafloor deformation (Tsushima et al., 2009; Lin et al., 2020). The inversion does not consider the geophysical process responsible for the modeled deformation (e.g., fault geometry, multi-fault ruptures, or non-seismic sources such as landslides). We invert sea level data from the three DART stations and the two near-field coastal sea level stations. The three DART stations and coastal sea level station SAND are given the same weight while station KING is allotted half of their weight, because higher weighting of KING led to numerically unstable inversions. Figure 4 shows the time intervals of the sea-level data used in the inversion as shaded gray regions. We regularize the inversion with a Tikhonov operator of zeroth order and then use an L-curve criterion from the inversions to find the optimal trade-off between smoothing and misfit (Figure S2, Aster et al., 2018).

The hydrodynamic solution clarifies that the vertical seafloor deformation necessary to produce the sea level observations is larger than the USGS model produces (1.4 m versus 0.4 m maximum displacement for models H0 and U0, respectively; Figures 4, 2). The tsunami waveform fits have an unweighted RMSE of 3.0 cm for model H0, one-third the value for model U0. Importantly, using model H0 as the initial condition in a fully non-hydrostatic trans-oceanic tsunami forward model produces good fits to the far-field tsunami wave-

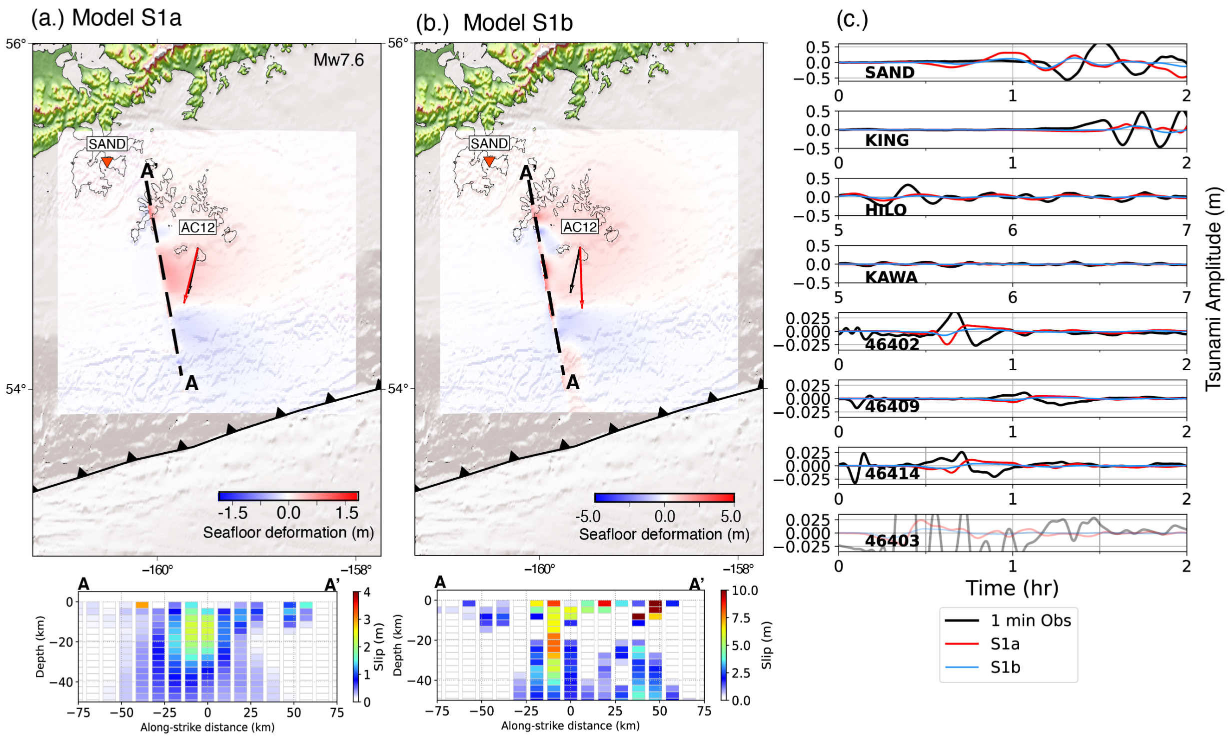

Figure 3 The results for model S1. (a.) Map of study area showing seafloor deformation implied by model S1a constrained to U.S. Geological Survey National Earthquake Information Center (USGS-NEIC) magnitude. Line A–A' shows the surface projection of the strike-slip geometry, with cross section A–A' below showing the modeled slip distribution along the strike-slip geometry. Model S1a is constrained to a moment magnitude ($\mathrm{M_w}$) of 7.6. (b.) Map of study area showing seafloor deformation implied by model S1b without any magnitude constraint, resulting in slip distribution equivalent to $\mathrm{M_w}$8.0. Line A–A' shows the surface projection of the strike-slip geometry, with cross section A–A' below showing the modeled slip distribution along the strike-slip geometry. (c.) Observed tsunami waveforms (black) with resulting synthetic waveforms from models in (a.) and (b.) shown in red and blue, respectively. This map was constructed using GMT 6 (Wessel et al., 2019).

forms tsunami waveforms at Hilo and Kawaihae (Figure 4b), observations that were not used in the inversion itself. Critically, the primary seafloor deformation signal resulting from model H0 is trench-parallel (Figure 4a), which is inconsistent with the expected pattern for a trench-perpendicular strike-slip fault. This pattern does not definitively rule out strike-slip faulting altogether but indicates that deformation from the strike-slip geometry is not the dominant signal for tsunami generation. Checkerboard tests of the hydrodynamic inversion reveal that the resolution is low across the inversion area, so some smearing of the main inversion features is to be expected, especially in the regions of smaller signals (Figure S3). Finally, we find that the trench-parallel deformation is well constrained by the Simeonof rupture zone (Figure 4a inset).

We describe a notable feature of the DART data included in this inversion. Sea level data in the deep ocean from a megathrust rupture can usually be conceptualized as a solitary Gaussian lump; DART station 46402's observed signal exemplifies this typical character (Figure 4). However, the sea level records at DART stations 46414 and 46409 are more complex. These stations contain what appears to be two partially overlapping Gaussian signals; the first requiring a smaller-amplitude source and the second requiring a larger source arriving after the first, indicating kinematic complexity of the tsunami source.

Model H0 has an apparent secondary signal that is neither trench-parallel nor trench-perpendicular. The signal area is dominated by a zone of subsidence to the north, with a concentrated area of uplift immediately to its south (Figure 4a inset, outlined in black). This positive–negative dipole pattern is reminiscent of a submarine landslide signal. The area is located on the steep part of the shelf-break and occurs somewhere within an area of $\sim 1300\,\mathrm{km}^2$; however, because the model resolution is low, this feature may be smeared, and the true size may be smaller. This apparent landslide signal is discussed in more detail in Section 5.2.

4 Allowing coeval megathrust and strike-slip rupture

4.1 Megathrust rupture initiation

Next, we consider the relative timing of rupture on this strike-slip and megathrust fault orientation. Megathrust rupture may have initiated coincident with strike-slip rupture or may have been initiated by dynamic triggering from the strike-slip rupture. We consider DART, coastal sea level, and static GNSS sites to compute a suite of slip models testing potential locations for megathrust initiation. The data weights are the same as in model S1, wherein DART station and static GNSS data were weighted 10 times higher than the coastal sea level station data. Our first model assumes megathrust

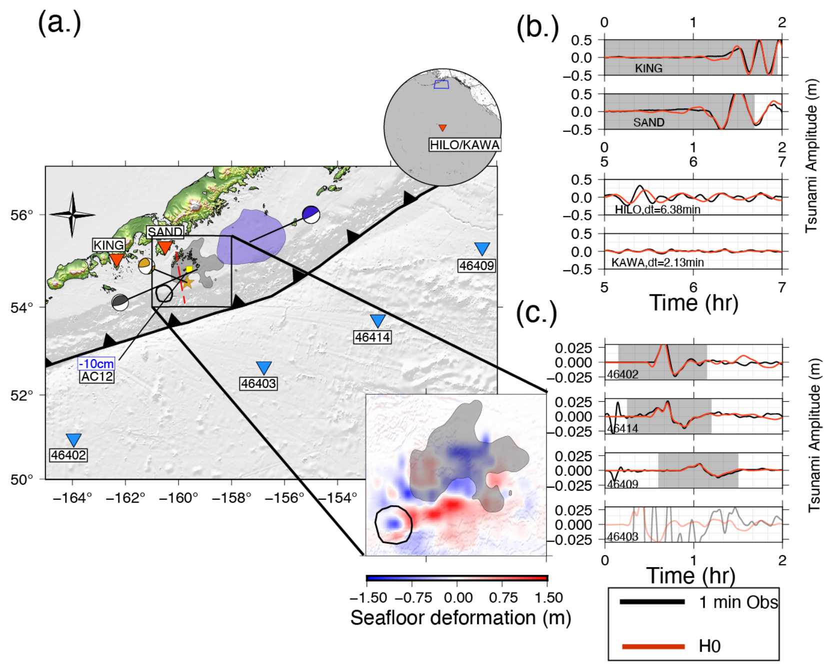

Figure 4 The hydrodynamic model (model H0) results. (a.) Region map with the 2020 Simeonof and 2021 Chignik rupture zones and associated W-Phase centroid moment tensors (WCMTs) shown in black and blue, respectively (Crowell and Melgar, 2020; USGS Earthquake Hazards Program, 2017). The surface projection of the U.S. Geological Survey National Earthquake Information Center (USGS-NEIC) finite fault plane for the 2020 Sand Point earthquake is delineated by a dashed red line. The epicenter and WCMT for the 2020 Sand Point earthquake are shown in gold. The King cove (KING) and Sand Point (SAND) sea level stations are shown as red triangles. Deep-ocean Assessment and Reporting of Tsunamis (DART) stations are shown as light blue triangles. Global Navigation Satellite System (GNSS) station AC12 location is the yellow square. The red dashed line shows the surface trace for the W-Phase nodal plane used in the USGS-NEIC finite fault model. The top inset shows the locations of the coastal sea level stations in Hawaii (red triangles) and the outline of the main study area is in blue. The bottom inset shows the modeled seafloor deformation (model H0). The black outline denotes an area where a suspected submarine landslide may have occurred, based on the classic dipole sea surface deformation pattern. (b.) The tsunami waveforms (observations in black, model synthetics in red) from the coastal sea level stations. Modeled waveforms for Hilo and Kawaihae (KAWA) are shifted by $6.38\,\mathrm{min}$ and $2.13\,\mathrm{min}$, respectively, for temporal consistency with the observed data. (c.) The tsunami waveforms (observations in black, model synthetics in red) from the DART stations. Gray shaded regions in (a.) and (b.) outline the portions of the coastal sea level and DART observations used in the tsunami inversion. This map was constructed using GMT 6 (Wessel et al., 2019).

initiation coincident with the NEIC event hypocenter (model S2a, nucleation point N0 in Figure 5a). Nine additional models consider a grid of potential megathrust nucleation points surrounding the hypocenter (models S2b): three nucleation points are to the west of the strike-slip fault where the megathrust is thought to be creeping (Li and Freymueller, 2018); three are along the intersection with the strike-slip fault; and three are to the east, within and up-dip from the 2020 Simeonof earthquake rupture zone (Crowell and Melgar, 2020) and in proximity to the contact of the 2020 Simeonof and 2021 Chignik rupture zones (Figure 5). We assume that dynamic triggering of the megathrust would take place when an S-wave front traveling from the hypocenter at $3.0\,\mathrm{km/s}$ reaches the nucleation site. We do not model the full rupture kinematics, rather we assume a constant rupture velocity from the nucleation point across the megathrust, such that slip on each subfault occurs instantaneously upon the passing of the rupture front. This assumption is valid because of the slow tsunami propagation speeds relative to earthquake slip durations (e.g., Williamson et al., 2019).

Low megathrust rupture propagation speeds are consistent with observations of "tsunami earthquakes", those seismic sources that produce larger amplitude tsunamis than expected for their magnitude. Slow rupture propagation may also explain a dearth of high-frequency ($\sim 1\,\mathrm{Hz}$) energy related to the megathrust, and therefore, difficulty in observing the source with typical seismic monitoring tools. To that end, we consider megathrust rupture speeds between $0.50\,\mathrm{km/s}$ and $1.25\,\mathrm{km/s}$. We assume the strike-slip plane ruptures at more traditional speeds, allowing a maximum rupture velocity of $3\,\mathrm{km/s}$.

We calculate the weighted RMSE for each combination of nucleation point and rupture velocity to determine the most likely scenario. Instantaneous, coincident rupture of both the strike-slip and megathrust geometries (model S2a) results in a weighted RMSE of $82.3\,\mathrm{cm}$ (Figure 5b). The minimum weighted RMSE ($77.8\,\mathrm{cm}$) occurs for the scenario of megathrust rupture initiation at a location $79\,\mathrm{km}$ southwest of the event hypocenter and propagating at $1\,\mathrm{km/s}$ toward the northeast of the proposed rupture domain (location N3, Figure 5). These results show that the observations are best explained by delayed initiation (dynamic triggering) of

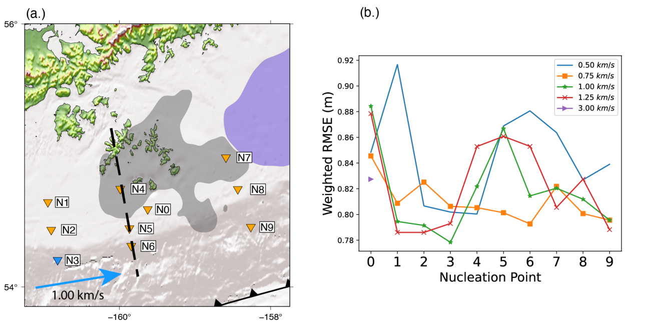

Figure 5 Potential megathrust rupture nucleation points. (a.) Map view of potential nucleation points (orange triangles), including event hypocenter (N0) and nine additional potential nucleation points (N1–N9). Preferred nucleation point, N3, is shown in blue along with the direction and best fitting speed of propagation, $1\,\mathrm{km/s}$. The 2020 Simeonof and 2021 Chignik rupture zones are shown in black and blue, respectively (Crowell and Melgar, 2020; USGS Earthquake Hazards Program, 2017). (b.) The weighted root mean squared error (RMSE) for static triggering at nucleation point N0 compared to RMSEs of nucleation points N1–N9 for four different rupture velocities. This map was constructed using GMT 6 (Wessel et al., 2019).

the megathrust, rather than coincident rupture of the strike-slip and megathrust geometries (Figures 5 and 6).

4.2 Full kinematic rupture modeling

We have demonstrated that the tsunami observations can allow for slip on both a strike-slip fault and the subduction interface. On its face, however, megathrust rupture seems incongruous with the WCMT produced by the NEIC that prefers a strike-slip rupture. The WCMT is calculated to idealize the earthquake as a point source and is therefore insensitive to complex slip, including multiple causative faults. Ultimately, the sum of slip contributed from any combination of faults must be consistent with the overall observed WCMT. Following the Monte Carlo approach of Yeck et al. (2023), we determine a right-lateral strike-slip fault geometry, that when combined with the megathrust geometry (strike/dip/rake: $245°/20°/90°$ from Hayes et al., 2018) of similar seismic moment, is consistent with the WCMT. The necessary right-lateral strike-slip geometry is similar in strike ($\sim 350°$) but much steeper in dip ($\sim 85°$) than the originally inferred strike-slip geometry (Figure S4). We note a caveat of this analysis: because we infer slow rupture speeds on the megathrust (Figure 5b), a typical WCMT solution may not equally sample the contributions from both geometries. Therefore, we interpret this analysis simply as evidence that the true strike-slip orientation may be steeper-dipping, with less constrained strike and dip. Some trial and error is used to find a model that is reasonably consistent with the overall WCMT.

We explore the earthquake source that best describes all available observations (teleseismic, near-field seismic, and geodetic), while allowing slip on the megathrust and steeply-dipping strike-slip plane (Figure S4). We use the Wavelet and simulated Annealing SliP (WASP) software package (Koch et al., 2024), a nonlinear simulated annealing method to model slip amplitude, rake, rupture time, and rise time in the wavelet domain (Ji et al., 2002; Koch et al., 2019; Goldberg et al., 2022). The two planes are divided into $10\,\mathrm{km} \times 10\,\mathrm{km}$ subfaults. The strike-slip geometry is composed of 15 subfaults in the along-strike direction and 7 in the down-dip direction for a total of 105 subfaults. The megathrust geometry contains 20 subfaults in the along-strike direction and 15 in the down-dip direction for a total of 300 subfaults. These kinematic models (referred to as K1–3) follow the results of the S2 models by prescribing delayed rupture initiation at point N3 on the megathrust orientation (Figure 5). We calculate the Kagan angle to compare the similarity between the model moment tensor and the WCMT (Figure 7); a lower Kagan angle implies better agreement with the moment tensor double-couple component (d'Amico et al., 2011). WASP was designed to jointly invert data from a variety of earthquake-observing instruments, including broadband teleseismic, regional strong-motion accelerometer, GNSS, and/or interferometric synthetic aperture radar observations (Goldberg et al., 2022). For application to the Sand Point event, we extend the software's capability to allow for DART sea level observations by transforming the sea level Green's functions calculated in GeoClaw to the frequency domain (refer to Section 2).

Models K1–3 consider both near-field and teleseismic observations of the earthquake, in addition to the DART tsunami observations. The earthquake observations include 42 teleseismic P waves, 16 telseismic SH waves, and 53 long-period surface waves (15 Love waves and 38 Rayleigh waves), as well as regional data from 6 strong-motion accelerometers, 13 high-rate GNSS stations, and 11 static GNSS stations. The high-rate GNSS data were processed with `GipsyX` (Bertiger et al., 2020). The teleseismic broadband and near-field accelerometer data processing are described in Goldberg et al. (2022) and Koch et al. (2019). Teleseismic observations are considered such that P waves receive half the weight of surface waves, and SH waves receive half the weight of P waves (e.g., Goldberg et al., 2022).

The K models have progressively longer allowable rise times (Table 1), as K1 and K2 kept selecting the longest allowable for their permitted ranges along the subduction zone interface. Results for K1 and K2 are given in Text S1. We focus on results from model K3, which we suggest has the most appropriate allowable rise times with "standard" rise times (up to $30\,\mathrm{s}$) along the strike-slip geometry and "very long" rise times (up to $120\,\mathrm{s}$) along the megathrust. The resulting model prefers slip equivalent to an $\mathrm{M_w}$7.6 rupture occurring on the strike-slip geometry with a rupture duration of $\sim 40\,\mathrm{s}$ (Figure 8). The megathrust takes much longer to rupture, $>300\,\mathrm{s}$ for a major portion of the subduction interface. The total slip on the megathrust is equivalent to an $\mathrm{M_w}$7.8 rupture with peak slip of $4.5\,\mathrm{m}$. The total resulting magnitude of both the strike-slip and megathrust orientations is $\mathrm{M_w}$7.9. The synthetic fit quality of the teleseismic arrivals is consistent with the weighting scheme applied, with surface waves being best fit and SH waves being poorly fit. Synthetic P waves for sta-

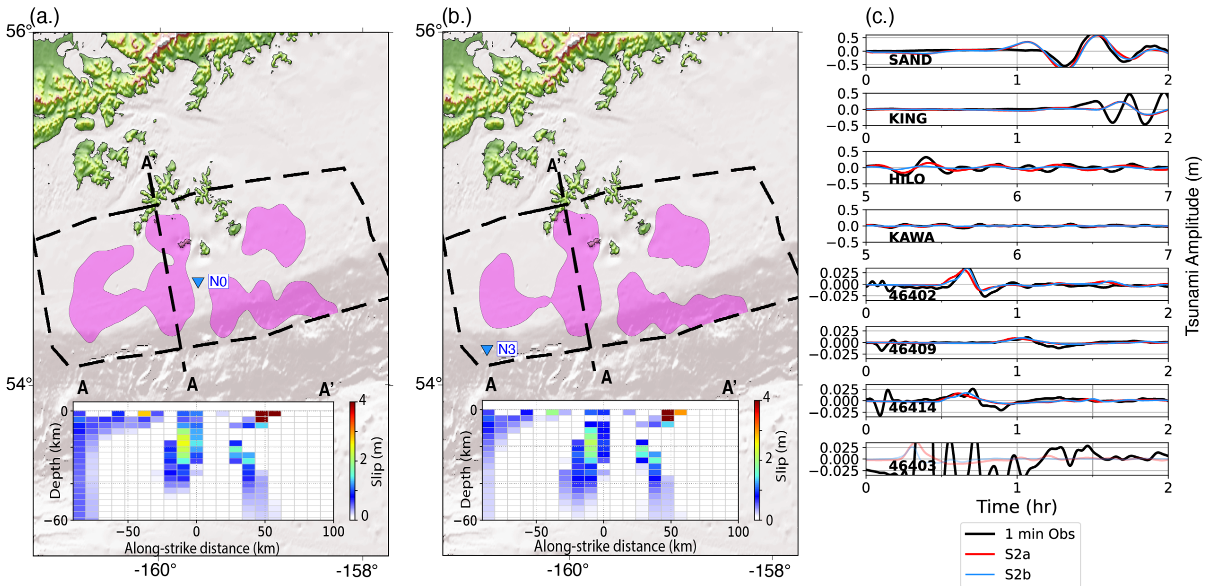

Figure 6 Model S2 results. (a.) Results of model S2a. Dashed black line delineates the portion of the megathrust considered in the inversion. Nucleation point N0 (event hypocenter) is shown as a blue inverted triangle. Magenta contour and shaded area shows the $>1\,\mathrm{m}$ rupture patch of the inversion rupture zone. Dashed line A–A' shows the surface projection of the strike-slip plane, with slip distribution on the strike-slip plane shown below. The maximum allowable rupture speed is $1.25\,\mathrm{km/s}$ for the megathrust and $3.0\,\mathrm{km/s}$ for the strike-slip plane. (b.) Results of preferred model S2b (nucleation point N3 with maximum allowable rupture velocity of $1\,\mathrm{km/s}$). Dashed black line delineates the portion of the megathrust considered in the inversion. Magenta contour and shaded area shows the $>1\,\mathrm{m}$ rupture patch of the inversion rupture zone. Nucleation point N3 is shown as a blue inverted triangle. A–A' is the surface projection of the strike-slip plane from the U.S. Geological Survey National Earthquake Information Center (USGS-NEIC) W-Phase centroid moment tensor (WCMT). (c.) The observed tsunami waveforms (black) compared to the modeled tsunami waveforms from models S2a and S2b in red and blue, respectively. This map was constructed using GMT 6 (Wessel et al., 2019).

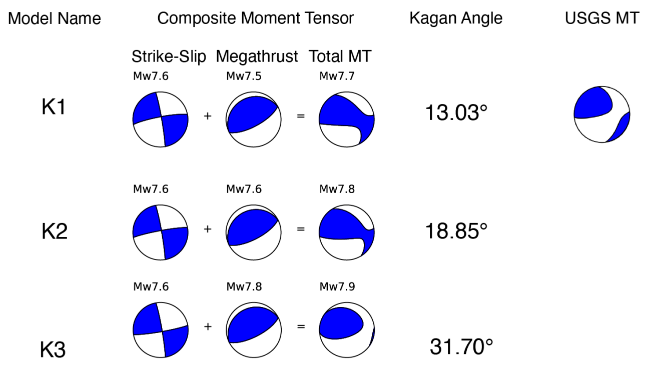

Figure 7 The associated moment tensors (MTs) for the strike-slip segment and megathrust segment for the four kinematic inversions and their composite MTs. The Kagan angle between each composite MT and the US. Geological Survey National Earthquake Information Center (USGS-NEIC) W-Phase centroid moment tensor (WCMT) are given for each inversion model. The USGS-NEIC MT is shown for visual comparison.

tions between $0°$ and $40°$ azimuth are low in amplitude compared to the observed waveforms (Figure S5). First arrivals improve considerably between azimuths of $60°$ and $110°$ but degrade again beyond that range. The synthetic Love and Rayleigh surface waves fit the shape and timing of the waveform packets yet are higher in amplitude than the observed waveforms (Figures S6 and S7). SH body waves fit the observed waveforms poorly, which is expected given their lower weights (Figure S8). High-rate GNSS waves for stations between azimuths $330°$ and $25°$ roughly follow the wave packet shape, yet they consistently underpredict the observed ground motion. Stations outside those azimuths are poorly fit (Figure S9). The strong motion synthetic fits to the observed data are moderately fit (Figure S10). Model K3 fits the observations at DARTs 46409 and 46414 well (Figure 8e). However, the solitary Gaussian lump at DART station 46402 arrives 4 minutes early in model K3 compared to the observed data. The coastal sea level station fit for Sand Point is moderate the synthetic tsunami signal arrives 2 minutes early and with poor fit to the first arrival; however, later arrivals are more consistent with the observations. The observations at the King Cove, Alaska, site remain poorly fit, with the synthetic waveforms severely underpredicting the observed sea level. The coastal sea level fits for the stations in Hawaii are good, though slightly underestimated (Figure 8e).

5 Discussion

5.1 Hidden megathrust rupture

The variety of inversions conducted in this study lead to a definitive conclusion: it is infeasible that a strike-slip mechanism alone caused the tsunami observed following the 2020 Sand Point earthquake. Therefore, we posit that, in addition to strike-slip rupture, a slow rup-

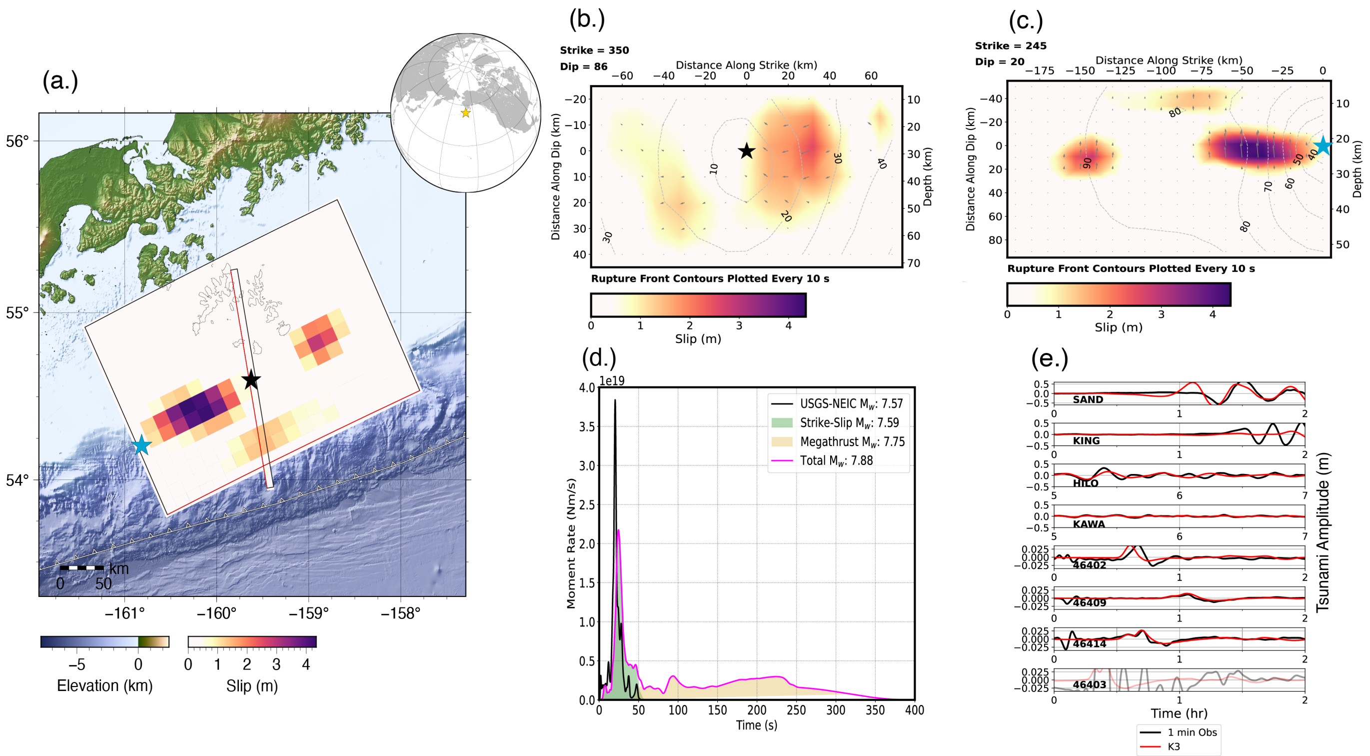

Figure 8 Model K3 results. (a.) Map showing the geographical distribution of slip along the megathrust as well as the strike-slip geometry used in inversion K3. Black star shows the hypocenter for the strike-slip, and a blue star shows the nucleation point for the megathrust. Red lines indicate the up-dip edge of the two fault orientations. (b.) Smoothed slip distribution and rupture time contours for the strike-slip segment. Small gray arrows indicate rake direction, scaled by amplitude of slip. Black star shows the hypocentral location. (c.) Same as (b.) but for the megathrust segment. Note that the rupture time contours start $29.5\,\mathrm{s}$ later, as we assume delayed slip to nucleation point N3, given by the blue star. (d.) The source time function for the published U.S. Geological Survey National Earthquake Information Center (USGS-NEIC) finite fault product (black; USGS Earthquake Hazards Program, 2017), the strike-slip segment of model K3 (green), the megathrust portion of model K3 (yellow), and the total source time function of model K3 (magenta) (e.) Observed (black) and model K3 synthetic (red) tsunami waveforms. This map was constructed using GMT 6 (Wessel et al., 2019).

ture on the adjacent megathrust occurred as part of the earthquake. We recognize that this theory is somewhat at odds with teleseismic source characterization carried out shortly after the event, such as that performed by the USGS NEIC; it would require a large amount of slip to go undetected by traditional rapid characterization techniques. Although we cannot fully account for how such a large quantity of slip could go undetected, we hypothesize that the slow megathrust slip radiates energy inefficiently at frequencies relevant to rapid response practices. It has been noted that near-trench "tsunami earthquakes" rupturing through the shallow, low rigidity portions of the megathrust can be depleted of both far-field (Newman et al., 2011) and near-field (Sahakian et al., 2019) seismic radiation. A characteristic of these tsunami earthquakes is very slow rupture (e.g., Riquelme and Fuentes, 2021). Our kinematic inversion results indicate that a slow rupture speed for the megathrust, $\sim 1\,\mathrm{km/s}$, is preferred; however, regional ground motion intensities were not anomalously low for an $\mathrm{M_w}$7.6, nor was far field radiated energy. These seemingly conflicting observations may be explained by the strike-slip rupture ($\mathrm{M_w}$7.6) radiating with the usual efficiency and the megathrust rupture ($\mathrm{M_w}$7.8) radiating inefficiently. Explaining the larger seismic moment of model K3 compared to the moment of the USGS-NEIC solution ($\mathrm{M_w}$7.9 vs. $\mathrm{M_w}$7.6, respectively) is an outstanding challenge. However, we note that there is some precedent for a large-magnitude rupture evading traditional seismic response algorithms. A recent example of this is the 2021 Sandwich Islands sequence (Jia et al., 2022). That sequence consisted of multiple large, complex events occurring in close spatiotemporal proximity, which led to initial underestimation of the overall moment release, in which the USGS NEIC initially reported as an $\mathrm{M_w}$7.5 event, only to decipher the larger magnitude $\mathrm{M_w}$8.1 mainshock, hidden in the coda of that first earthquake, the following day. While we have been unable to find similar evidence of a larger rupture hidden in the coda of the teleseismic data from the 2020 Sand Point event, the possibility remains that further scrutiny of the data may illuminate some previously undetected seismic signal. Another tsunamigenic possibility is that rupture progresses at a more "traditional" speed and that tsunamigenesis occurs as a result of inelastic wedge deformation (Ma and Nie, 2019). This mechanism is feasible for Sand Point because most of the Shumagin segment is creeping in the interseismic period (Li and Freymueller, 2018) and thus can reasonably be inferred to prefer rate-strengthening modes of rupture. Indeed, Crowell and Melgar (2020) imaged some after-slip following the Simeonof earthquake. In this process, the rupture front propagates at a traditional speed, near shear-wave speeds, but very long rise times allow slip to accumulate slowly. These processes could ostensibly be enough to keep the true extent of the megathrust co-seismic slip 'silent' in the seismic data.

5.2 Potential submarine landslide

Finally, we note that none of the slip inversions considered in this work have been able to fit the tsunami waveforms at the King Cove coastal sea level station (Figures 2c, 3c, 6c, 8e). In addition, models K1–K3 had a notable timing misfit to DART station 46402 (e.g., Figure 8e, S11e, S18e). Recall that the hydrodynamic model (H0) showed evidence for a submarine landslide in the southwestern corner of the model space (Figure 4a), which we hypothesize may be necessary to improve fits to King Cove coastal sea level station and DART station 46402. Submarine landslides produce a positive-negative dipole of seafloor deformation, wherein the negative portion (subsidence) corresponds to the area where mass is removed and the positive lobe corresponds to the area where the excavated mass moves downslope (e.g., Williamson et al., 2019). The location of such a dipole signal is highlighted in Figure 4a. This area is on the steep section of the shelf-break and is within 20 km of the ALEUT-05 active source survey (Bécel et al., 2017). That study noted widespread evidence that this part of the continental slope is prone to submarine landslides. Thus, we posit that a submarine landslide could have contributed to the observed tsunami, particularly the signal observed at King Cove. However, we note that the occurrence of a submarine landslide can only be confirmed by direct observation, for example by repeated multibeam bathymetry surveys. We consider the cumulative effect of the kinematic earthquake slip model K3 with the submarine landslide signal observed in model H0 (Figure 9). We assume the submarine landslide occurs instantaneously, 180 s after earthquake origin, based on trial-and-error testing of landslide onset at various times after earthquake origin. While the fits to the King Cove waveform do improve with the addition of the landslide, the degradation of fits to DART station 46402 shows the limitations of the assumption of an instantaneous landslide (Figure 9). In reality, landslides occur over many seconds — thought to be on the order of ~100 s (Ten Brink et al., 2006). However, accounting for temporal evolution of the landslide is beyond our scope.

5.3 Regional context and hazard considerations

The 2020 Sand Point earthquake shares some critical similarities with the 1946 M_w8.6 earthquake on the neighboring Sanak segment. The 1946 event was highly deficient in seismic radiation, with a teleseismic magnitude of only 7.4, indicating there may be some structural control on the megathrust that generates slow and long ruptures devoid of seismic radiation (López and Okal, 2006). Furthermore, López and Okal (2006) showed that the 1946 Sanak ruptured at a velocity of

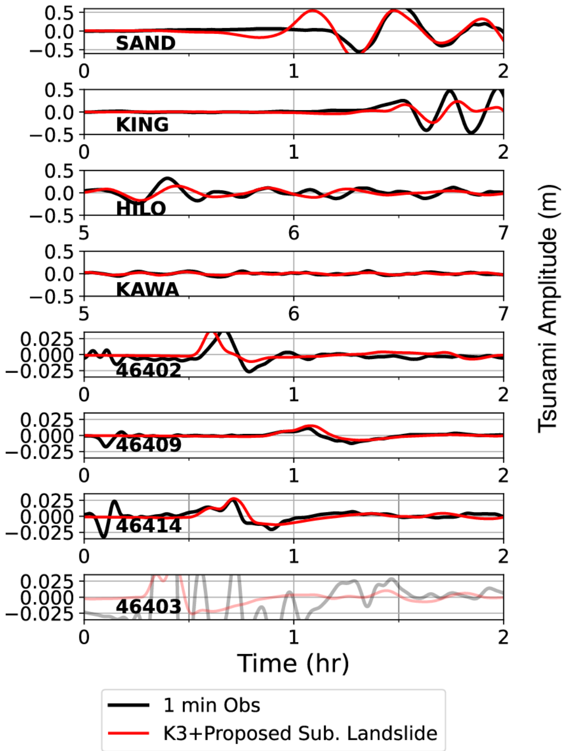

Figure 9 The observed tsunami waveforms (black) compared to synthetic tsunami waveforms (red) resulting from the combination of kinematic model K3 and a submarine landslide signal obtained from model H0.

1.12 km/s and required a submarine landslide to fit near-field tsunami data, mirroring what we propose here. Bécel et al. (2017) demonstrated that the Shumagin segment contains complex tsunamigenic structures and demonstrated that the small frontal prism and heterogeneous plate interface at shallow depth are prone to slow earthquakes. These factors may contribute to slow rupture velocities and large rise times in this area of the megathrust. In fact, Tanioka et al. (1997) postulated that rupture could proceed in an erratic manner in the presence of a sediment starved corrugated interface. Both the 2020 Sand Point and 1946 Sanak earthquakes are poorly described by teleseismic data. López and Okal (2006) ascribed this feature to destructive interference in all azimuths for surface waves due to the directivity of the rupture and the limitations of historical instrument records to measure waves free from directivity effects. However, this limitation does not affect present day instrumentation. We posit that the source of this discrepancy could instead be due to the slow speed of rupture and slow rise times caused by the features described in Bécel et al. (2017). The similarities between the 1946 Sanak and 2020 Sand Point earthquakes may also extend to their coupling environment. Herman and Furlong (2021) show that spatial variations in displacements caused by coupling between the overriding plate and slab in the 1938 Semidi rupture area, and low coupling throughout the Shumagin segment, would likely cause large right-lateral shear stresses in the section of the segment that produced the strike-slip component of the 2020 Sand Point earthquake. The presence of a strike-slip plane may help illuminate the state of locking in this region of the megathrust. We posit that the dynamic triggering of the megathrust by the strike-slip component of the earthquake occurred in a region of low coupling (Figure 5, Li and Freymueller, 2018). Low coupling would allow shear waves to cause displacements large enough to promote rupture in this region. The rupture front would then propagate unilaterally to the northeast into a region of potentially higher coupling and higher slip deficits where it would eventually stop (Li and Freymueller, 2018; Xiao et al., 2021). Coseismic slip along the megathrust propagating from the southwest to northeast of the proposed rupture area is consistent with the Sand Point rupture arresting at the boundary of the July 2021 Chignik rupture area (Figure 10). The western downdip edge of the 2020 Sand Point rupture area also appears to delineate the edge of rupture of the July 2023 $\mathrm{M_w}$7.2 Sand Point earthquake.

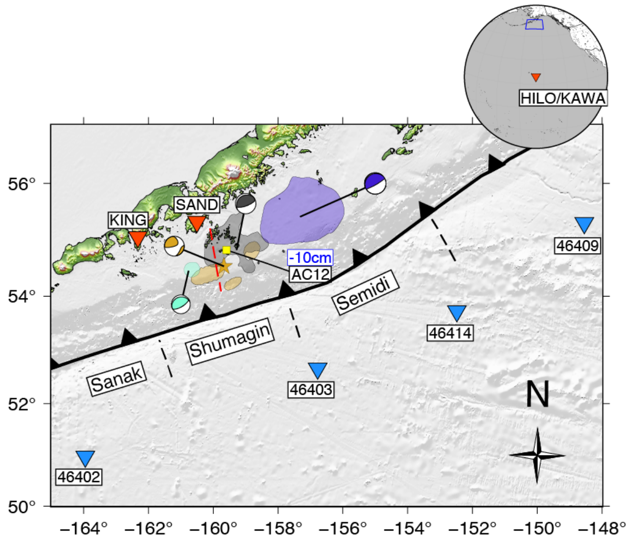

Figure 10 The proposed rupture zone for the 2020 Sand Point megathrust is shown in gold. The 2020 Simeonof rupture zone from Crowell and Melgar (2020) is shown in black, the 2021 Chignik rupture zone from the U.S. Geological Survey National Earthquake Information Center (USGS-NEIC) finite fault model for the event is shown in dark blue, and the rupture area for the July 15, 2023, Sand Point earthquake from the USGS-NEIC finite fault model is shown in aquamarine. The surface projection of the strike-slip plane associated with the 2020 Sand Point earthquake is delineated by a dashed red line. The King cove (KING) and Sand Point (SAND) sea level stations are shown in red. Deep-ocean Assessment and Reporting of Tsunamis (DART) stations are shown as light blue triangles. The amount of subsidence at Global Navigation Satellite System (GNSS) station AC12 (yellow square) for the 2020 Sand Point earthquake is shown to be $10\,\mathrm{cm}$. The inset shows the locations of the coastal sea level stations in Hawaii (red triangles). The blue box shows the location of the main study area. This map was constructed using GMT 6 (Wessel et al., 2019).

The total magnitude of the two-segment rupture from model K3 is $\mathrm{M_w}$7.9 ($\mathrm{M_o} = 8.38 \times 10^{20}\,\mathrm{N\,m}$), $\mathrm{M_w}$7.6 on the strike-slip segment and $\mathrm{M_w}$7.8 on the megathrust. DeSanto et al. (2023) observed with offshore GNSS-acoustic data that the megathrust remained partially locked after the $\mathrm{M_w}$7.8 Simeonof earthquake and that it potentially held unrelieved strain up-dip from the rupture zone. Xiao et al. (2021) found that the amount of slip deficit left to rupture after the 2020 Simeonof earthquake, up-dip from the rupture zone (Figure 7 of Xiao et al., 2021), is equivalent to a $\mathrm{M_w}$7.8. Our work therefore seems to suggest that the Sand Point earthquake may have nearly exhausted the remaining slip deficit on the megathrust up-dip from the Simeonof rupture zone. However, we note that our proposed megathrust slip is off-centered from the Simeonof rupture zone and does not include slip up-dip of $20\,\mathrm{km}$.

Checkerboard tests show that this portion of the inversion is well resolved in the hydrodynamic model but that there is also appreciable smearing in the slip inversion (Figure S3). So, whether the un-ruptured sections of the Shumagin segment will experience post-seismic relaxation, leading to decreased hazards, or continue to be loaded as a source of future tsunamigenic events to the Aleutian communities in this region is uncertain.

6 Conclusion

We have shown that a strike-slip fault geometry alone is inadequate for generating the tsunami observed following the October 2020 Sand Point, Alaska, earthquake. Using hydrodynamic, static slip, and kinematic slip inversions, we find that there was likely slip along the megathrust in addition to strike-slip faulting. The sea surface deformation necessary to recreate the tsunami waveforms at the Alaskan and Hawaiian sea level stations, as well as the DART stations, requires slip consistent with the megathrust orientation. Our final model indicates that slip on a steeply-dipping strike-slip plane dynamically triggers slip on the megathrust $\sim 30\,\mathrm{s}$ after event origin time at a location $79\,\mathrm{km}$ southwest of the event hypocenter. While the strike-slip plane ruptures at typical speeds (up to $3\,\mathrm{km/s}$), the megathrust likely ruptures at a much slower velocity of $1\,\mathrm{km/s}$. The model results in slip equivalent to an $\mathrm{M_w}$7.6 on the strike-slip plane and $\mathrm{M_w}$7.8 on the megathrust plane, for a cumulative slip equivalent to an $\mathrm{M_w}$7.9 earthquake. We hypothesize that the slow megathrust rupture does not contribute much seismic radiation — much like the 1946 Sanak earthquake — allowing it to go largely unnoticed in traditional teleseismic response. The rupture front propagates at low velocity into a region of high slip deficit up-dip from the $\mathrm{M_w}$7.8 Simeonof earthquake but does not slip up-dip of $\sim 20\,\mathrm{km}$. Finally, we hypothesize that a submarine landslide explains the tsunami waveforms at the King Cove coastal sea level station and DART station 46402.

7 Acknowledgments

We would like to thank Diego Arcas for helpful discussions. We would like to thank the USGS internal reviewers and two anonymous peer reviewers for their helpful feedback on this paper. This work was partially funded by NSF OAC grant No. 1835661 and NASA DISASTERS grant 80NSSC19K1104. Any use of trade, firm, or product names is for descriptive purposes only and does not

imply endorsement by the U.S. Government.

8 Data and code availability

The USGS event page for the 2020 Sand Point earthquake is available at https://earthquake.usgs.gov/earthquakes/eventpage/us6000c9hg. The water level data for the DART stations can be obtained from the DART website (https://www.ndbc.noaa.gov/dart.shtml) and for the coastal water level stations can be obtained from NOAA's CO-OPS' Environmental Research Division's Data Access Program (ERDDAP) server (https://opendap.co-ops.nos.noaa.gov/erddap/index.html). The vertical offset for AC12 was obtained from the GAGE Facility operated by the EarthScope Consortium (UNAVCO Community, 2008). The sea level inversion code is available from GitHub (https://github.com/ssantellanes/water-level-inversion) and is archived on Zenodo at Santellanes et al. (2021). The static slip inversions were generated using the FakeQuakes code, which is part of the MudPy source modeling toolkit available on GitHub (https://github.com/dmelgarm/MudPy); the latest version is archived on Zenodo at Melgar et al. (2021). The WASP kinematic inversion code is available at Koch et al. (2024). Strong motion accelerometer data and broadband data are available from the SAGE Facility operated by the EarthScope Consortium (formerly IRIS) Data Management Center (https://ds.iris.edu/ds/nodes/dmc/data/types/waveform-data). High-rate and static Global Navigation Satellite System data are available from the GAGE Facility operated by the EarthScope Cosortium (formerly UNAVCO, Inc.; https://data.unavco.org/archive/gnss/highrate/ and https://gage-data.earthscope.org/archive/gnss/products/event). This material is based on services provided by the GAGE Facility, operated by UNAVCO, Inc., with support from the National Science Foundation, the National Aeronautics and Space Administration, and the U.S. Geological Survey under NSF Cooperative Agreement EAR-1724794. The data, models, and supplementary figures in this study are available in a USGS ScienceBase data release (Santellanes et al., 2025).

References

Aster, R., Borchers, B., and Thurber, C. *Parameter estimation and inverse problems*. Elsevier, Cambridge, MA, 2018. doi: 10.1016/C2015-0-02458-3.

Bécel, A., Shillington, D. J., Delescluse, M., Nedimović, M. R., Abers, G. A., Saffer, D. M., Webb, S. C., Keranen, K. M., Roche, P.-H., Li, J., and Kuehn, H. Tsunamigenic structures in a creeping section of the Alaska subduction zone. *Nature Geoscience*, 10(8):609–613, Aug. 2017. doi: 10.1038/ngeo2990.

Bertiger, W., Bar-Sever, Y., Dorsey, A., Haines, B., Harvey, N., Hemberger, D., Heflin, M., Lu, W., Miller, M., Moore, A. W., Murphy, D., Ries, P., Romans, L., Sibois, A., Sibthorpe, A., Szilagyi, B., Vallisneri, M., and Willis, P. GipsyX/RTGx, a new tool set for space geodetic operations and research. *Advances in Space Research*, 66(3):469–489, Aug. 2020. doi: 10.1016/j.asr.2020.04.015.

Crowell, B. W. and Melgar, D. Slipping the Shumagin Gap: A Kinematic Coseismic and Early Afterslip Model of the Mw 7.8 Simeonof Island, Alaska, Earthquake. *Geophysical Research Letters*, 47(19), Oct. 2020. doi: 10.1029/2020GL090308.

d'Amico, S., Orecchio, B., Presti, D., Gervasi, A., Zhu, L., Guerra, I., Neri, G., and Herrmann, R. Testing the Stability of Moment Tensor Solutions for Small Earthquakes in the Calabro-Peloritan Arc Region (Southern Italy). *Bollettino di Geofisica Teorica ed Applicata*, 2011. doi: 10.4430/bgta0009.

Davies, J., Sykes, L., House, L., and Jacob, K. Shumagin Seismic Gap, Alaska Peninsula: History of great earthquakes, tectonic setting, and evidence for high seismic potential. *Journal of Geophysical Research*, 86(B5):3821, 1981. doi: 10.1029/JB086iB05p03821.

DeSanto, J. B., Webb, S. C., Nooner, S. L., Schmidt, D. A., Crowell, B. W., Brooks, B. A., Ericksen, T. L., and Chadwell, C. D. Limited Shallow Slip for the 2020 Simeonof Earthquake, Alaska, Constrained by GNSS-Acoustic. *Geophysical Research Letters*, 50 (16):e2023GL105045, Aug. 2023. doi: 10.1029/2023GL105045.

Goldberg, D. E., Koch, P., Melgar, D., Riquelme, S., and Yeck, W. L. Beyond the Teleseism: Introducing Regional Seismic and Geodetic Data into Routine USGS Finite-Fault Modeling. *Seismological Research Letters*, 93(6):3308–3323, Nov. 2022. doi: 10.1785/0220220047.

Hayes, G. P., Moore, G. L., Portner, D. E., Hearne, M., Flamme, H., Furtney, M., and Smoczyk, G. M. Slab2, a comprehensive subduction zone geometry model. *Science*, 362(6410):58–61, Oct. 2018. doi: 10.1126/science.aat4723.

Herman, M. W. and Furlong, K. P. Triggering an unexpected earthquake in an uncoupled subduction zone. *Science Advances*, 7 (13):eabf7590, Mar. 2021. doi: 10.1126/sciadv.abf7590.

Herring, T. A., Melbourne, T. I., Murray, M. H., Floyd, M. A., Szeliga, W. M., King, R. W., Phillips, D. A., Puskas, C. M., Santillan, M., and Wang, L. Plate Boundary Observatory and related networks: GPS data analysis methods and geodetic products. *Reviews of Geophysics*, 54(4):759–808, Dec. 2016. doi: 10.1002/2016RG000529.

Ji, C., Wald, D. J., and Helmberger, D. V. Source Description of the 1999 Hector Mine, California, Earthquake, Part I: Wavelet Domain Inversion Theory and Resolution Analysis. *Bulletin of the Seismological Society of America*, 92(4):1192–1207, May 2002. doi: 10.1785/0120000916.

Jia, Z., Zhan, Z., and Kanamori, H. The 2021 South Sandwich Island *M_w* 8.2 Earthquake: A Slow Event Sandwiched Between Regular Ruptures. *Geophysical Research Letters*, 49(3), Feb. 2022. doi: 10.1029/2021GL097104.

Koch, P., Bravo, F., Riquelme, S., and Crempien, J. G. F. Near-Real-Time Finite-Fault Inversions for Large Earthquakes in Chile Using Strong-Motion Data. *Seismological Research Letters*, Aug. 2019. doi: 10.1785/0220180294.

Koch, P., Goldberg, D. E., Hunsinger, H. E., Melgar, D., Riquelme, S., Yeck, W. L., and Haynie, K. L. Wavelet and simulated Annealing SliP inversion (WASP), U.S. Geological Survey software release, 2024. doi: 10.5066/P1EKKUNW.

Larson, K. M., Lay, T., Yamazaki, Y., Cheung, K. F., Ye, L., Williams, S. D., and Davis, J. L. Dynamic Sea Level Variation From GNSS: 2020 Shumagin Earthquake Tsunami Resonance and Hurricane Laura. *Geophysical Research Letters*, 48(4), Feb. 2021. doi: 10.1029/2020GL091378.

LeVeque, R. J., George, D. L., and Berger, M. J. Tsunami modelling with adaptively refined finite volume methods. *Acta Numerica*, 20:211–289, May 2011. doi: 10.1017/S0962492911000043.

Li, S. and Freymueller, J. T. Spatial Variation of Slip Behavior Beneath the Alaska Peninsula Along Alaska-Aleutian Subduction Zone. *Geophysical Research Letters*, 45(8):3453–3460, Apr. 2018. doi: 10.1002/2017GL076761.

Lin, J.-T., Aslam, K. S., Thomas, A. M., and Melgar, D. Overlapping regions of coseismic and transient slow slip on the Hawaiian décollement. *Earth and Planetary Science Letters*, 544:116353, Aug. 2020. doi: 10.1016/j.epsl.2020.116353.

Liu, C., Lay, T., Xiong, X., and Wen, Y. Rupture of the 2020 M_W 7.8 Earthquake in the Shumagin Gap Inferred From Seismic and Geodetic Observations. *Geophysical Research Letters*, 47(22), Nov. 2020. doi: 10.1029/2020GL090806.

Liu, C., Lay, T., and Xiong, X. The 29 July 2021 M_W 8.2 Chignik, Alaska Peninsula Earthquake Rupture Inferred From Seismic and Geodetic Observations: Re-Rupture of the Western 2/3 of the 1938 Rupture Zone. *Geophysical Research Letters*, 49(4), Feb. 2022. doi: 10.1029/2021GL096004.

López, A. M. and Okal, E. A. A seismological reassessment of the source of the 1946 Aleutian 'tsunami' earthquake. *Geophysical Journal International*, 165(3):835–849, June 2006. doi: 10.1111/j.1365-246X.2006.02899.x.

Ma, S. and Nie, S. Dynamic Wedge Failure and Along-Arc Variations of Tsunamigenesis in the Japan Trench Margin. *Geophysical Research Letters*, 46(15):8782–8790, Aug. 2019. doi: 10.1029/2019GL083148.

Melgar, D. and Bock, Y. Near-field tsunami models with rapid earthquake source inversions from land- and ocean-based observations: The potential for forecast and warning: TSUNAMI MODELS WITH RAPID INVERSIONS. *Journal of Geophysical Research: Solid Earth*, 118(11):5939–5955, Nov. 2013. doi: 10.1002/2013JB010506.

Melgar, D., LeVeque, R. J., Dreger, D. S., and Allen, R. M. Kinematic rupture scenarios and synthetic displacement data: An example application to the Cascadia subduction zone. *Journal of Geophysical Research: Solid Earth*, 121(9):6658–6674, 2016. doi: 10.1002/2016JB013314.

Melgar, D., Lin, T., Kong, Q., Christineruhl, and Marfito, B. dmelgarm/MudPy: v1.3, Sept. 2021. doi: 10.5281/ZENODO.5397091.

Newman, A. V., Hayes, G., Wei, Y., and Convers, J. The 25 October 2010 Mentawai tsunami earthquake, from real-time discriminants, finite-fault rupture, and tsunami excitation: THE 2010 MENTAWAI TSUNAMI EARTHQUAKE. *Geophysical Research Letters*, 38(5):n/a–n/a, Mar. 2011. doi: 10.1029/2010GL046498.

Okada, Y. Surface deformation due to shear and tensile faults in a half-space. *Bulletin of the Seismological Society of America*, 75(4):1135–1154, 1985. doi: https://doi.org/10.1785/BSSA0750041135.

Pasyanos, M. E., Masters, T. G., Laske, G., and Ma, Z. LITHO1.0: An updated crust and lithospheric model of the Earth. *Journal of Geophysical Research: Solid Earth*, 119(3):2153–2173, Mar. 2014. doi: 10.1002/2013JB010626.

Riquelme, S. and Fuentes, M. Tsunami Efficiency Due to Very Slow Earthquakes. *Seismological Research Letters*, 92(5):2998–3006, Sept. 2021. doi: 10.1785/0220200198.

Sahakian, V., Melgar, D., and Muzli, M. Weak Near-Field Behavior of a Tsunami Earthquake: Toward Real-Time Identification for Local Warning. *Geophysical Research Letters*, 46(16):9519–9528, Aug. 2019. doi: 10.1029/2019GL083989.

Santellanes, S., Lin, J.-T., and Melgar, D. ssantellanes/water-level-inversion: First release, Sept. 2021. doi: 10.5281/ZENODO.5498175.

Santellanes, S. R., Goldberg, D. E., Koch, P., Melgar, D., Yeck, W. L., Crowell, B. W., and Lin, J.-T. 2025, Supporting Data and Models for An unexplained tsunami: Was there megathrust slip during the 2020 Mw7.6 Sand Point, Alaska, earthquake?: U.S. Geological Survey data release,, 2025. doi: https://doi.org/10.5066/P9G8ODEH.

Tanioka, Y., Ruff, L., and Satake, K. What controls the lateral variation of large earthquake occurrence along the Japan Trench? *The Island Arc*, 6(3):261–266, Sept. 1997. doi: 10.1111/j.1440-1738.1997.tb00176.x.

Ten Brink, U. S., Geist, E. L., and Andrews, B. D. Size distribution of submarine landslides and its implication to tsunami hazard in Puerto Rico. *Geophysical Research Letters*, 33(11): 2006GL026125, June 2006. doi: 10.1029/2006GL026125.

Titov, V. V., Gonzalez, F. I., Bernard, E. N., Eble, M. C., Mofjeld, H. O., Newman, J. C., and Venturato, A. J. Real-Time Tsunami Forecasting: Challenges and Solutions. *Natural Hazards*, 35(1):35–41, May 2005. doi: 10.1007/s11069-004-2403-3.

Tozer, B., Sandwell, D. T., Smith, W. H. F., Olson, C., Beale, J. R., and Wessel, P. Global Bathymetry and Topography at 15 Arc Sec: SRTM15+. *Earth and Space Science*, 6(10):1847–1864, Oct. 2019. doi: 10.1029/2019EA000658.

Tsai, V. C., Ampuero, J.-P., Kanamori, H., and Stevenson, D. J. Estimating the effect of Earth elasticity and variable water density on tsunami speeds: ELASTIC COMPRESSIBLE TSUNAMI SPEED. *Geophysical Research Letters*, 40(3):492–496, Feb. 2013. doi: 10.1002/grl.50147.

Tsushima, H., Hino, R., Fujimoto, H., Tanioka, Y., and Imamura, F. Near-field tsunami forecasting from cabled ocean bottom pressure data. *Journal of Geophysical Research*, 114(B6):B06309, June 2009. doi: 10.1029/2008JB005988.

USGS Earthquake Hazards Program. Advanced National Seismic System (ANSS) Comprehensive Catalog, 2017. doi: 10.5066/F7MS3QZH. Publisher: U.S. Geological Survey.

Wessel, P., Luis, J. F., Uieda, L. a., Scharroo, R., Wobbe, F., Smith, W. H., and Tian, D. The generic mapping tools version 6. *Geochemistry, Geophysics, Geosystems*, 20(11):5556–5564, 2019. doi: 10.1029/2019GC008515.

Williamson, A., Melgar, D., and Rim, D. The Effect of Earthquake Kinematics on Tsunami Propagation. *Journal of Geophysical Research: Solid Earth*, 124(11):11639–11650, Nov. 2019. doi: 10.1029/2019JB017522.

Witter, R. C., Briggs, R. W., Engelhart, S. E., Gelfenbaum, G., Koehler, R. D., and Barnhart, W. D. Little late Holocene strain accumulation and release on the Aleutian megathrust below the Shumagin Islands, Alaska. *Geophysical Research Letters*, 41(7): 2359–2367, Apr. 2014. doi: 10.1002/2014GL059393.

Xiao, Z., Freymueller, J. T., Grapenthin, R., Elliott, J. L., Drooff, C., and Fusso, L. The deep Shumagin gap filled: Kinematic rupture model and slip budget analysis of the 2020 Mw 7.8 Simeonof earthquake constrained by GNSS, global seismic waveforms, and floating InSAR. *Earth and Planetary Science Letters*, 576: 117241, Dec. 2021. doi: 10.1016/j.epsl.2021.117241.

Yeck, W. L., Shelly, D. R., Materna, K. Z., Goldberg, D. E., and Earle, P. S. Dense geophysical observations reveal a triggered, concurrent multi-fault rupture at the Mendocino Triple Junction. *Communications Earth & Environment*, 4(1):94, Mar. 2023. doi: 10.1038/s43247-023-00752-2.

Yue, H., Lay, T., Li, L., Yamazaki, Y., Cheung, K. F., Rivera, L., Hill, E. M., Sieh, K., Kongko, W., and Muhari, A. Validation of linearity assumptions for using tsunami waveforms in joint inversion of kinematic rupture models: Application to the 2010 Mentawai M_w 7.8 tsunami earthquake. *Journal of Geophysical Research: Solid Earth*, 120(3):1728–1747, Mar. 2015. doi: 10.1002/2014JB011721.